RSC Advances

ROYAL SOCIETY OF CHEMISTRY

www.rsc.org/advances

Spin-resolved transport properties in zigzag α-graphyne nanoribbons with symmetric and asymmetric edge fluorinations

Dan Zhang[a], Mengqiu Long[a,b,*], Xiaojiao Zhang[c], Jun Ouyang[a], Hui Xu[a], and KowkSum Chan[b,*]

[a]*Institute of Super-microstructure and Ultrafast Process in Advanced Materials, School of Physics and Electronics, Central South University, Changsha 410083, China*

[b]*Department of Physics and Materials Science, City University of Hong Kong, Hong Kong, China*

[c]*Physical Science and Technology College of Yichun University, Yichun 336000, China*

Abstract: Using the non-equilibrium Green's function method and the spin-polarized density functional theory, we investigate the stability and spin-resolved electronic transport properties of zigzag α-graphyne nanoribbons (ZαGYNRs) with symmetric (F-ZαGYNRs-F) and asymmetric (F2-ZαGYNRs-F) edge fluorinations. Our results show edge fluorination can enhance the stability of ZαGYNRs. The spin-resolved transport calculations reveal that the devices of F-ZαGYNRs-F with odd ribbon widths behave as a conductor with a linear current-voltage relationship, while the semiconductor property and perfect bipolar spin-filtering effect can be observed in those devices with even ribbon widths. In contrast, the spin-resolved transport properties of the asymmetric edge fluorinated F2-ZαGYNRs-F systems are independent of the ribbon width. Moreover, the F2-ZαGYNRs-F device is a perfect spin device with nearly 100% bipolar spin-filtering and spin negative differential resistance effect in a wide bias voltage region. And the magnetoresistance effect with the order of 10^6 and the spin rectification ratio as high as 10^8 have also been predicted. These phenomena suggest ZαGYNRs with asymmetric edge fluorination can be considered as a promising candidate material for nano-electronics and spintronics.

Keywords: zigzag α-graphyne nanoribbons; non-equilibrium Green's function; bipolar spin-filtering effect; rectifying effect; magnetoresistance effect

---

[*] Corresponding authors.
E-mail addresses: mqlong@csu.edu.cn (M. Long), apkschan@cityu.edu.hk (K. Chan).

Introduction

After the successful preparation of graphene[1] and the discovery of its distinctive properties[2-5], a new kind of carbon allotrope, graphyne, has also attracted intensive attentions[6-8]. Graphyne, which is predicted by Baughman *et al.*[6], is the first non-natural carbon allotropes consisting of both *sp* and *sp^2* hybridization. It can be obtained by replacing some carbon-carbon (C-C) *sp^2* bonds in graphene with acetylenic (*i.e.* single- and triple-bond) linkages. In graphyne, the presence of *sp* and *sp^2* hybridization, uniformly distributed pores, density much smaller than that of graphene and tunable electronic properties are considered as promising characteristics for applications in nanoelectronics. More importantly, graphyne has many allotropes[6,9], such as α-graphyne, β-graphyne, γ-graphyne, and graphdiyne. It has been demonstrated that these graphynes are assumed to be chemically stable[10]. In 2010, large area films of graphdiyne have been successfully fabricated on copper surface by a cross-coupling reaction using hexaethynylbenzene[11], which is a big step towards the preparation of graphynes, and attracts many studies on graphdiyne and its related structures[12-16].

α-graphyne, one of the graphyne allotropes, is a zero-gap semiconductor[17,18]; its two-dimensional (2D) structure has direction-dependent Dirac cones[19], and has attracted many theoretical studies[20-26]. To broaden its practical applications in the fields of electronics and spintronics, an energy gap and magnetism are needed. Similar to graphene nanoribbons (GNRs)[2,27,28], α-graphyne can also be tailored into nanoribbons[29], and can be mainly classified into two types: armchair α-graphyne nanoribbons (AαGYNRs) and zigzag α-graphyne nanoribbons (ZαGYNRs). Calculations have indicated that all AαGYNRs are nonmagnetic (NM), and the band gap oscillates with a period of three when the ribbon width increases[29]. While the ZαGYNRs have a stable antiferromagnetic (AFM) configuration, and the band structure are spin degenerate[9,29].

There are many previous studies which demonstrated that the edge states have a significant effect on the nanoribbons' electronic and magnetic properties[30-34], and also, fluorination can stabilize the structure and modulate the edge states of the nanoribbons[33,35,36]. Therefore, in this letter, we want to study the edge symmetric and asymmetric fluorination for the purpose of tuning the electronic structure and transport properties of ZαGYNRs. The

theoretical techniques used are the non-equilibrium Green's function (NEGF) method and the spin-polarized density functional theory (DFT). Our results show that the perfect spin-filtering effect, spin negative differential resistance (SNDR) effect, spin rectifying effect, and giant magnetoresistance (MR) can be realized in a wide bias region in ZαGYNRs with asymmetric fluorination systems. However, the transport properties of the ZαGYNRs with symmetric fluorination are dependent on the ribbon width, and the ribbons with even ribbon width also have perfect spin-filtering effect.

Models and methods

The ZαGYNRs are originally obtained by cutting 2D α-graphyne along zigzag lines, and according to the number (n) of zigzag carbon chains along the nanoribbon' axis, ZαGYNRs can be named as nZαGYNRs. For the purpose of studying the symmetry-dependent properties of ZαGYNRs devices[20], the ZαGYNRs with the ribbon width of 4 (symmetric, 2.26nm) and 5 (asymmetric, 2.86nm) as examples have been selected in our calculation. The edges are saturated by fluorine (F) atoms to enhance the stability and meanwhile remove the dangling bonds. In this letter, two kinds of edge fluorination are considered: symmetric fluorination (each edge saturated by one F atom) and asymmetric fluorination (one of the edges saturated by one F atom and the other saturated by two F atoms). Here, we do not consider the edge dihydrogenated 4ZαGYNR and 5ZαGYNR due to the non-magnetic properties. And all the models considered are the devices of F-4ZαGYNRs-F, F-5ZαGYNRs-F, F2-4ZαGYNRs-F, and F2-5ZαGYNRs-F, denoted as M1, M2, M3 and M4 for brevity, respectively. The left panels of Figs. 1(a) and (b) present the two-lead systems of M1 and M2, and the right panels of Figs. 1(a) and (b) are the side view of M1, M3 and M2, M4, respectively. The left and right electrodes are semi-infinite F-4ZαGYNRs-F (F2-4ZαGYNRs-F) along the z direction in M1 (M3), and they are semi-infinite F-5ZαGYNRs-F (F2-5ZαGYNRs-F) in M2 (M4).

For the two-lead systems, which can be seen in Fig. 1, the spin-dependent transport properties are studied by the Atomistix ToolKit package[37-39], which is based on the spin DFT and the NEGF method. In our calculation, the real space grid technique is used with the energy cutoff of 300 Ry as the required cutoff energy in numerical integrations. The spin generalized gradient approximation with Perdew-Burke-Ernzerh form of functions is

employed for the exchange-correlation potential (our test by using Perdew-Burke-Ernzerh and hybrid functional HSE06 with Vienna ab-initio simulation package (VASP) give a similar band structure of a-graphyne unit cell). The k-point grid 1, 1, and 100 are used in the x, y, z direction, respectively, where z is the direction of electron transport. Open boundary conditions are used to describe the electronic and transport properties of the devices. A vacuum layer of 16 Å is added in x and y directions to avoid the interaction between adjacent ribbons. The wave functions of all the atoms are expanded by double-zeta polarized basis set. The temperature of the electrodes is set to be 300 K. The geometrical structures are fully optimized in the presence of the two-leads until the residual force on each atom is smaller than 0.01 eV/Å. The spin-polarized current through the system is calculated using the Landauer-Büttiker formula[40],

$$I_\sigma\left(V_b\right) = \frac{e}{h}\int_{\mu_R(V_b)}^{\mu_L(V_b)}\left\{T_\sigma\left(E,V_b\right)\left[f_L\left(E,V_b\right) - f_R\left(E,V_b\right)\right]\right\}dE \tag{1}$$

Here e is the electron charge, h is the Planck's constant, and T_σ is the transmission of an electron with spin σ. $f_{L(R)}\left(E,V_b\right)$ is the Fermi-Dirac distribution function of the left (right) electrode, and $\mu_{L(R)}\left(V_b\right)$ is the chemical potential of the left (right) electrode, which depends on the external bias voltage, V_b. T_σ is obtained from the equation,

$$T_\sigma\left(E,V_b\right) = Tr\left[\text{Im}\left\{\sum_{L_\sigma}^r\left(E,V_b\right)\right\}G_\sigma^r\left(E,V_b\right) \times \text{Im}\left\{\sum_{R_\sigma}^r\left(E,V_b\right)\right\}G_\sigma^a\left(E,V_b\right)\right] \tag{2}$$

Here $G^r\left(G^a\right)$ is the retarded (advanced) Green's function matrix, and $\sum_L^r\left(\sum_R^r\right)$ is the retarded self-energy matrix for the left (right) electrode.

Results and discussion

Firstly, we present an analysis of the stability of different fluorination configurations. The formation energy is defined by the following formula,

$$E_{form} = E_{ribbon+F}^{tol} - E_{ribbon}^{tol} - \frac{1}{2}N_F E_{F_2} \tag{3}$$

Here, $E_{ribbon+F}^{tol}$, E_{ribbon}^{tol}, N_F, and E_{F_2} represent the total energy of the edge fluorinated ZαGYNR, the total energy of the bare edged ZαGYNR, the number of F atoms, and the energy of the isolated F_2 molecule, respectively. The optimized lattice constant is 6.98 Å. And

the calculated formation energies of F-4ZαGYNR-F, F-5ZαGYNR-F, F2-4ZαGYNR-F, and F2-5ZαGYNR-F unit cells are -6.769 eV, -6.776 eV, -8.625 eV, and -8.499 eV, respectively. One can readily note that the formation energies of the edge saturated geometries are all negative, which means that all the edge fluorinated ZαGYNRs are more stable than the edge unsaturated ones. We also calculated the formation energy of H-4ZαGYNR-H (-3.571 eV) and O-4ZαGYNR-O (-6.161 eV), find fluorination are the most stable one, which is similar to that of GNR[33,35].

In the two-lead system, the spin orientation of the left (right) electrode can be controlled by an external magnetic field[41,42], which plays an important role in spintronic devices[20]. Here, we use M_L and M_R to represent the magnetizations of the left and right electrodes, M_L and M_R can be set to 1, 0 or -1, corresponding to a magnetization along the +y direction, nonmagnetic, and a magnetization along the -y direction, respectively. The following two configurations, $[M_L, M_R] = [1, 1]$ and $[M_L, M_R] = [1, -1]$ have been chosen. $[M_L, M_R]$ = [1, 1] means the spin orientations of the left and right electrodes are in a parallel configuration (PC), while $[M_L, M_R]$ = [1, -1] means the spin orientations of the left electrode and right electrode are in an antiparallel configuration (APC)[43]. And for APC, a more rigorous scheme involving noncollinear spin-polarization configuration would need to be considered. According to previous studies, the noncollinear spin polarization has only a minor influence on the transmission spectrum of GNR and αGYNR, and neglecting this effect would be reasonable[20,41]. Thus, we will utilize the collinear spin in this work.

Fig. 2 shows the currents as a function of the applied bias voltage (I-V curves) for the four devices in APC and PC. For M1 and M2 in APC, as shown in Fig. 2(a), the I-V curves exhibit different characteristics. That of M1 presents semi-conductive properties with a threshold voltage of 0.06 V. It can be noted that the spin-down current only appears in positive bias, meanwhile the spin-up current only appears in negative bias, which indicates M1 has a perfect bipolar spin-filtering effect and can be act as spin-diode. The variation of the spin current with the increase of |V_b| goes through three different stages: the current is nearly zero when |V_b| is lower than 0.06 V, the system shows a linear I-V curve when 0.06 V < |V_b| < 0.3

V, and the current is saturated when $|V_b|$ is higher than 0.3 V. While for M2 in APC, one can find that the spin-up and spin-down I-V curves (the blue and purple lines in Fig. 2(a)) have overlapped, and displays the Ohmic characteristic.

When M1 and M2 are in PC, the corresponding I-V curves are shown in Fig. 2(b), we can note that the I-V curves of both spin for M1 increase sharply and then remain at the saturated values with the increase of $|V_b|$, and the spin-up current is slightly smaller than the spin-down current. In M2, it is clear that the I-V curve for PC is nearly the same as that of APC (as shown in Figs. 2(a) and (b)), which indicates that the spin configuration of the electrodes has little effect on the I-V characteristics of M2.

We also plot the I-V curves of M3 and M4 in APC and PC (Figs. 2(c)-(d)). Obviously, it exhibit similar characteristics for M3 and M4 in the same spin configuration, while the different I-V curves are obtained for different spin configurations. For M3 (or M4) in APC, as shown in Fig. 2 (c), when the bias voltage is positive, the spin-down current firstly increase to the biggest value at 0.4 V and then decrease with the increase of V_b. So the NDR effect can be observed in the spin-down current, while the spin-up current is always suppressed. In the negative bias region, the spin-up current firstly increases to the biggest value at around 0.4 V and then decrease with the increase of V_b, with the spin-down current being always suppressed. Therefore, the SNDR, bipolar spin-filtering and spin-rectifying behaviors are observed in M3 and M4 with APC. Furthermore, for the PC situation, as shown in Fig. 2(d), we can see both the spin-up and spin-down currents are much smaller than that in the APC, and the NDR behaviors can also be found.

Spin-filtering efficiency (SFE) is one of the most important parameters for spin-filter devices. To understand quantitatively the spin-polarization characteristic of the devices M1, M3 and M4, we calculate the SFEs defined as, $SFE = \left[\left(I_\uparrow - I_\downarrow \right) / \left(I_\uparrow + I_\downarrow \right) \right] \times 100\%$. Fig. 3(a) shows the SFEs of M1, M3 and M4 in APC in the bias range of [-0.6, -0.1 V]. We note that the SFEs are all above 90% in the bias range of [-0.5, -0.1V], and can even reach 100% in some bias voltages. Fig. 3(b) shows the SFEs of M1, M3 and M4 in the positive bias range of [0.1, 0.6 V], one can find the spin flip phenomenon, and each one of the SFEs also higher than 90% in the bias range of [0.1, 0.5 V], which indicates M1, M3 and M4 are ideal bipolar

spin-filtering devices.

Moreover, to present the rectifying behavior in Fig. 2, the rectifying ratio has also been calculated using the formula, $R = \left|I(\pm V_b)\right|_{max} / \left|I(m V_b)\right|_{min}$. Fig. 3(c) shows the rectifying ratio of the spin-up current for M1, M3 and M4. It is noted that the rectifying ratio of M1 is smaller than those of M3 and M4. The maximum rectifying ratio of M3 can reach 10^7, and is 10^6 for M4. For the spin-down rectifying ratio, as shown in Fig. 3(d), one can see it is similar to the spin-up rectifying ratio, but the rectifying ratio of M4 can even reach the order of 10^8.

Comparing Fig. 2(c) with (d), it is clear that the magnetic configuration of the electrodes has a significant effect on the *I-V* curves of M3 and M4. The current of M3 (or M4) in the APC is much larger than that in the PC at low applied bias voltages, which give rise to a giant MR. According to $MR = \left(I_{APC} - I_{PC}\right)/I_{PC}$, where I_{APC} and I_{PC} indicate the currents in APC and PC, the MR of both devices in the [-0.6, -0.1 V] and [0.1, 0.6 V] bias regions have been calculated and shown in Figs. 3(e) and (f). We can find that there are very large MR for M3 and M4 in the bias range of [-0.3, -0.5 V] and [0.3, 0.5 V], and the maximum MR can even reach 10^6.

In order to understand the basic mechanism of the symmetry effect on the spin transport properties of the F-ZαGYNRs-F devices, Figs. 4(a) and (b) present the band structures of F-4ZαGYNR-F and F-5ZαGYNR-F. It is shown that there are two coupled subbands of spin-up and spin-down around the Fermi level, which respectively meet each other near the X point in the Brillouin zone and corresponding to bonding π and antibonding π^* subbands. Thus, we can expect that the characteristics of π and π^* would determine the transport properties of F-ZαGYNRs-F device. We also present the wave functions of the spin-up π and π^* subbands at the Γ point for F-4ZαGYNR-F and F-5ZαGYNR-F, as plotted in Figs. 4(a) and (b), respectively. It is found that the wave functions have different symmetric characteristics. For F-4ZαGYNR-F, the wave functions of π and π^* subbands have a σ mirror plane, and there are even and odd parity under the σ mirror operation, respectively. While for F-5ZαGYNR-F, the σ mirror plane is absent, which leads to the wave functions of π and π^* subbands have no definite parity.

A further understanding can be obtained from the band structures of the left (right)

electrode and the transport spectra, as shown in Figs. 4(d) and (e). For the spin-up state of M1 in APC, when a 0.4 V bias is applied, the bands of the left electrode shift downward, meanwhile the bands of the right electrode shift upward, as a result the antibonding π^* subband of the left electrode and the bonding π subband of the right electrode overlap with each other in the bias window (Fig. 4(e)). Owing to the π and π^* subbands have opposite parities with respect to the σ mirror operation, the electron transmission from the π^* subband of the left electrode to the π subband of the right electrode is forbidden. So a large zero transmission gap (ZTG) appears and no electron transmission contributes to the current. While for M2 (Fig. 4(d)), the overlap of the subbands between the two electrodes is similar to that of M1 within the bias window. However, as its π and π^* subbands have no definite parity, the electrons transmission from the π^* subband of the left electrode to the π subband of the right electrode are allowed. So a G_0 ($G_0 = e^2/h$ is the quantum conductance) conductance and linear current-voltage characteristic appears in Fig. 2(a). As the current is determined by the integral of $T(E,V_b)$ within the bias window (*Eq.*1), therefore, there are electron transmission that contributes to the spin-up current of M2, but no electron transmission contributes to that of M1, which leads to the spin-up current of M2 is much larger than that of M1.

Moreover, in order to have a clear picture about the mechanism on the spin configuration of the electrodes, as shown in Figs. 4(c) and (e), we give the band structures of the left and right electrodes, and the transmission spectra for M1 under 0.4 V bias voltages in PC and APC. The spin band structures of the left electrode and right electrode in APC are opposite, but that in PC are the same. So when a 0.4 V bias voltage is applied, taking the spin-up situation for example, it is found that the π^* subband of the left electrode overlaps with the π and π^* subbands of the right electrode of M1 in PC, since the π^* subbands of both electrodes have the same parity, so a transmission peak appears, the spin-up transport channel is opened. While for M1 in APC (in Fig4. (e)), the spin-up subbands between the left electrode and the right electrode are mismatched and results in the corresponding transport channel are closed.

To understand the spin transport properties of M3 and M4, the following we also give the band structures of F2-4ZαGYNR-F and F2-5ZαGYNR-F, as shown in Figs. 5(a) and (b). One can find that the edge saturated pattern has a great effect on the band structure of ZαGYNRs.

When the C atoms at one edge of the ZαGYNRs are saturated by two F atoms, and that of the other edge are saturated by one F atom, we can find the degeneracy of the π and π^* bands near the Fermi level disappears, and there are two separated spin-up and spin-down bands appearing near the Fermi level, which would determine the transport properties of F2-ZαGYNRs-F device under low bias voltage. Furthermore, we also present the nature of the wave functions of both subbands for the F2-4ZαGYNR-F and F2-5ZαGYNR-F, as plotted in Figs. 5(c) and (d). It is found that the wave functions also have no definite parity owing to the absent of the σ mirror plane.

To understand the mechanism of the perfect spin-filtering and the giant MR effects of F2-ZαGYNRs-F devices, we consider M3 as an example, as shown in Figs. 5(e) and (f), and present the band structure of the left electrode, transmission spectrum, and the band structure of the right electrode for M3 in the APC and PC at the bias of 0.4 V. From Fig. 5(e), it is clearly seen that when a positive bias of 0.4 V is applied, only the spin-down subbands of the left and right electrode are overlaps with each other in the bias window, so only the spin-down transmission peak appears. Therefore, only the spin-down transport channel is opened, and the spin-filtering effect appears. While in the PC situation, as shown in Fig. 5(f), one can find that only the spin-down subband of the left electrode and the spin-up subband of the right electrode appear in the bias window, resulting in a mismatch between the identical spin subbands. Thus a large ZTG appears in the bias window for each spin state, the transmission between the two electrodes is forbidden and the transport channel is closed. As a result, a significant current can flow in APC but it is suppressed in PC in the bias range of [0.1, 0.6 V], which leads to a large MR in the asymmetric edge fluorinated ZαGYNR devices.

Fig. 6 presents the electronic band structure, density of states (DOS) and projected density of states (PDOS) of F-4ZαGYNR-F and F2-4ZαGYNR-F to explain the origin of the different electronic characteristics between F-ZαGYNR-F and F2-ZαGYNR-F. From the middle panel of Fig. 6(a), we can see there are two peaks around the Fermi level in the DOS, which are caused by the degeneracy of spin-up (spin-down) π and π^* subbands around the X point. The PDOS can give a clear picture about the origin of the π and π^* subbands, as shown in the right panel of Fig. 6 (a), we can get the information that the two peaks around the Fermi level are mainly contributed by 1A carbons (showing in Fig. 6(b)). While for F2-4ZαGYNR-F,

the band structure is changed obviously (Fig. 6(c)). From the DOS as shown in the middle panel of Fig. 6 (c), we can see that the spin-down and spin-up DOS spectra are split around the Fermi level, where the spin-down DOS appears above the Fermi level, and the spin-up one appears below the Fermi level. Our PDOS show that the spin-up and spin-down bands around the Fermi level are mainly come from the 1B and 2A carbons of the edges (Fig. 6(d)), which indicates that the additional F atoms attached on the top edge induces a change of the boundary condition and an appearance of another type of edge state.

Furthermore, we also give the spin-resolved transmission spectra as a function of the electron energy and bias voltage for spin-down states of the devices in APC, as shown in Fig. 7. From Fig. 7(a), we can see that when the bias voltage is negative, the transmission is zero within the bias window, so the spin-down current is forbidden. But when the bias voltage is positive and larger than 0.06 V, the spin-down transmission peaks come into the bias window and contribute to the spin-down current. As a result, a spin rectification ratio can be found in M1. For M2, we can see the transmission coefficients are always $1G_0$ ($G_0 = e^2/h$ is the quantum conductance) in the whole bias window of [-0.6, 0.6 V], so the current increases linearly with the increase of $|V_b|$. Figs. 7(c) and (d) show the spin-resolved transmission spectra as a function of electron energy and bias voltage for spin-down states of M3 and M4 in APC. In the positive bias region, one can see that the integrated areas of the transmission coefficients within the bias window firstly increase and then decrease with the increase of $|V_b|$, and lead to the same trend in the current, so the SNDR behaviors can be found in M3 and M4. Meanwhile, in the negative bias window, the transport coefficient is nearly zero within the bias window, and a large spin rectification ratio appears.

Conclusions

In conclusion, using the DFT and the NEGF method, we have investigated the stability and spin-dependent electronic transport properties of ZαGYNRs with symmetric and asymmetric edge fluorinations in the APC and PC. Our results show that both F-ZαGYNRs-F and F2-ZαGYNRs-F geometries are stable. The F-ZαGYNRs-F device exhibits symmetry-dependent transport properties, which results from the different symmetries of the wave functions of the π and π^* subbands near the Fermi level for symmetric and asymmetric

F-ZαGYNRs-F. In APC, the symmetric F-4ZαGYNRs-F device shows a perfect bipolar spin-filtering effect, while the asymmetric F-5ZαGYNRs-F device behaves as conductors with linear *I-V* relationship. We also investigate the spin-dependent transport properties of F2-ZαGYNRs-F and the SNDR phenomenon, nearly 100% bipolar spin-filtering, and spin rectifying functions have been observed in both F2-4ZαGYNRs-F and F2-5ZαGYNRs-F devices in APC. What's more, a giant magnetoresistance as large as 10^6 can also be observed in both F2-4ZαGYNRs-F and F2-5ZαGYNRs-F devices. These results would be useful in the development of high performance graphyne-based spin filters and logic devices.

Acknowledgements

References

1 K.S. Novoselov, A.K. Geim, S.V. Morozov, D. Jiang, Y. Zhang, S.V. Dubonos, et al., *Science*, 2004, **306**, 666.

2 Y.W. Son, M.L. Cohen, and S.G. Louie, *Phys. Rev. Lett.*, 2006, **97**, 216803.

3 D.A. Abanin, S.V. Morozov, L.A. Ponomarenko, R.V. Gorbachev, A.S. Mayorov, M.I. Katsnelson, et al., *Science*, 2011, **332**, 328.

4 Z.Y. Li, H.Y. Qian, J. Wu, B.L. Gu, and W.H. Duan, *Phys. Rev. Lett.*, 2008, **100**, 206802.

5 W. Han and R.K. Kawakami, *Phys. Rev. Lett.*, 2011, **107**, 047207.

6 R.H. Baughman, H. Eckhardt, and M. Kertesz, *J. Chem. Phys.*, 1987, **87**, 6687.

7 Y.F. Li, D. Datta, Z.H. Li, V.B. Shenoy, *Comp. Mater. Sci.*, 2014, **83**, 212.

8 M. Inagaki and F.Y. Kang, *J. Mater. Chem. A*, 2014, **2**, 13193.

9 G.D. Yu, Z. Liu, W.Z. Gao, Y.S. Zheng, *J. Phys.: Condens. Matter*, 2013, **25**, 285502.

10 A.L. Ivanovskii, *Progress in Solid State Chemistry*, 2013, **41**, 1.

11 G.X. Li, Y.L. Li, H.B. Liu, Y.B. Guo, Y.J. Li, D.B. Zhu, *Chem. Commun.*, 2010, **46**, 3256.

12 H.Y. Zhang, M.W. Zhao, X.J. He, Z.H. Wang, X.J. Zhang, X.D. Liu, *J. Phys. Chem. C*, 2011, **115**, 8845.

13 B.G. Kim, H.J. Choi, *Phys. Rev. B*, 2012, **86**, 115435.

14 M.Q. Long, L. Tang, D. Wang, Y.L. Li, Z.G. Shuai, *ACS NANO*, 2011, **5**, 2593.

15 Y.H. Zhou, J. Zeng, K.Q. Chen, *Carbon*, 2014, **76**, 175.

16 Z.Z. Lin, Q. Wei, X.M. Zhu, *Carbon*, 2014, **66**, 504.

17 O. Leenaerts, B. Partoens, and F.M. Peeters, *Appl. Phys. Lett.*, 2013, **103**, 013105.

18 H.Q. Huang, W.H. Duan, and Z.R. Liu, *New Jour. Phys.*, 2013, **15**, 023004.

19 D. Malko, C. Neiss, F. Vñies, A. Görling, *Phys. Rev. Lett.*, 2012, **108**, 086804.

20 Q. Yue, S.L. Chang, J.C. Tan, S.Q. Qin, K. Jun, J.B. Li, *Phys. Rev. B*, 2012, **86**, 235448.

21 X.N. Niu, D.Z. Yang, M.S. Si, D.S. Xue, *J. Appl. Phys.*, 2014, **115**, 143706.

22 R. Longuinhos, E.A. Moujaes, S.S. Alexandre, R.W. Nunes, *Chem. Mater.*, 2014, **26**, 3701.

23 M.M. Xue, H. Qiu, W.L. Guo, *Nanotechnology*, 2013, **24**, 505720.

24 X.H. Deng, M.S. Si, J.Y. Dai, *J. Chem. Phys.*, 2012, **137**, 201101.

25 J.M. Chen, J.Y. Xi, D. Wang, Z.G. Shuai, *J. Phys. Chem. Lett.*, 2013, **4**, 1443.

26 V. Ongun Özçelik, and S. Ciraci, *J. Phys. Chem. C*, 2013, **117**, 2175.

27 V. Barone, O. Hod, G.E. Scuseria, *Nano Lett.*, 2006, **6**, 2748.

28 H. Lee, Y.W. Son, N. Park, S. Han, J. Yu, *Phys. Rev. B*, 2005, **72**, 174431.

29 Q. Yue, S.L. Chang, K. Jun, J.C. Tan, S.Q. Qin, J.B. Li, *J. Chem. Phys.*, 2012, **136**, 244702.

30 G. Lee, K. Cho, *Phys. Rev. B,* 2009, **79**, 165440.

31 B. Xu, J. Yin, Y.D. Xia, X.G. Wan, K. Jiang, Z.G. Liu, *Appl. Phys. Lett.*, 2010, **96**, 163102.

32 Y. Ding, Y.L. Wang, *Appl. Phys. Lett.*, 2012, **101**, 013102.

33 Y.L. Wang, Y. Ding, J. Ni, *Phys. Rev. B*, 2010, **81**, 193407.

34 D. Zhang, M.Q. Long, X.J. Zhang, C. Cao, H. Xu, M.J. Li, et al., *Chem. Phys. Lett.*, 2014, **616-617**, 178.

35 M. Maruyama, K. Kusakabe, *J. Phys. Soc. Jpn.*, 2004, **73**, 656.

36 K.N. Kudin, *ACS Nano*, 2008, **2**, 516.

37 J.P. Perdew, A. Zunger, *Phys. Rev. B*, 1981, **23**, 5048.

38 J. Taylor, H. Guo, J. Wang, *Phys. Rev. B*, 2001, **63**, 245407.

39 M. Brandbyge, J.L. Mozos, P. Ordejón, J. Taylor, K. Stokbro, *Phys. Rev. B*, 2002, **65**, 165401.

40 M. Büttiker, Y. Imry, R. Landauer, S. Pinhas, *Phys. Rev. B*, 1985, **31**, 6207.

41 W.Y. Kim, K.S. Kim, *Nature Nanotechnology*, 2008, **3**, 408.

42 W.H. Wang, K. Pi, Y. Li, Y.F. Chiang, P. Wei, J. Shi, et al., *Phys. Rev. B*, 2008, **77**, 020402(R).

43 Y.H. Zhou, J. Zeng, L.M. Tang, K.Q. Chen, W.P. Hu, *Organic Electronics*, 2013, **14**, 2940.

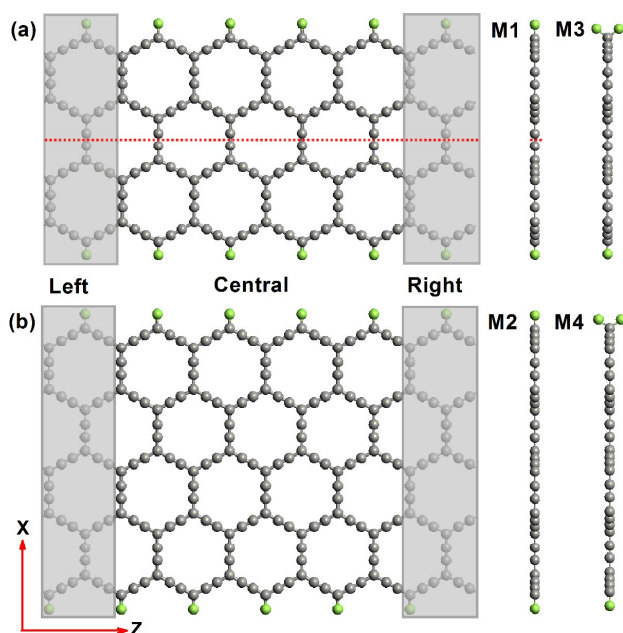# Figures

Fig. 1 Zhang et al.

Fig. 1 (Color online) Two-lead system of the ZαGYNR. The left panel of (a) and (b) are the front view of M1 and M2. The right panel figures are the side view of (a) M1, M3 and (b) M2, M4. Left, Central, Right represent the left electrode, central scattering region, right electrode, respectively. The red dashed line indicates the σ mirror plane. The gray and green balls represent C and F atoms respectively.
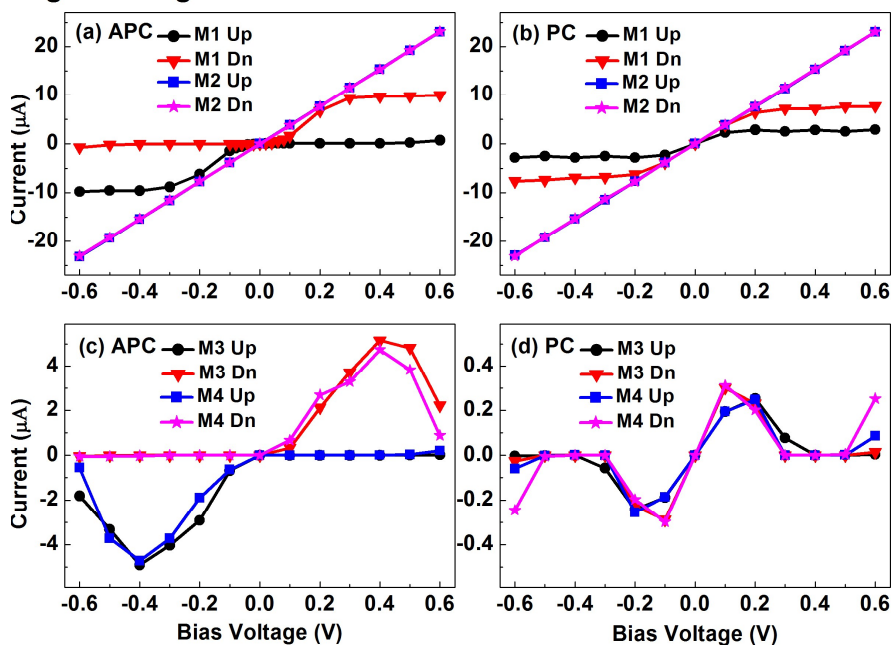

Fig. 2 Zhang et al.

Fig. 2 (Color online) I-V curves for the devices. (a) M1 and M2 in APC; (b) M1 and M2 in PC; (c) and (d) M3 and M4 in APC and PC, respectively.

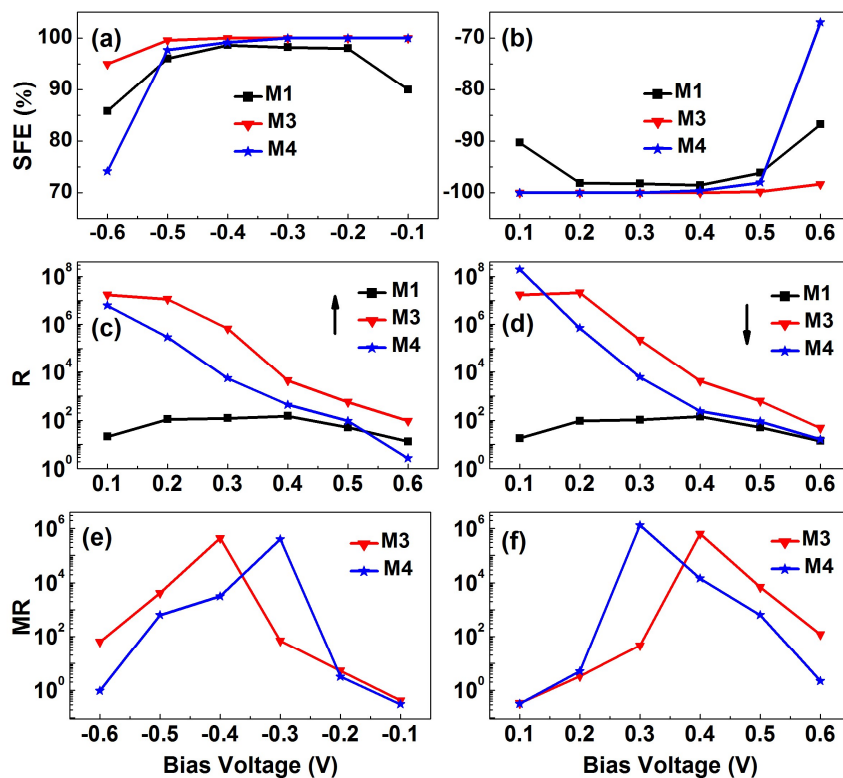13

Fig. 3 Zhang et al.

Fig. 3 (Color online) (a) and (b) Spin-filtering efficiency for M1, M3 and M4 in APC. (c) and (d) Log-scale of the rectifying ratio for the spin-up current and spin-down current of M1, M3 and M4 in APC, respectively. The two orientations of the black arrow denote the spin-up and spin-down situations. (e) and (f) Log-scale of the total MR versus the applied bias for M3 and M4.
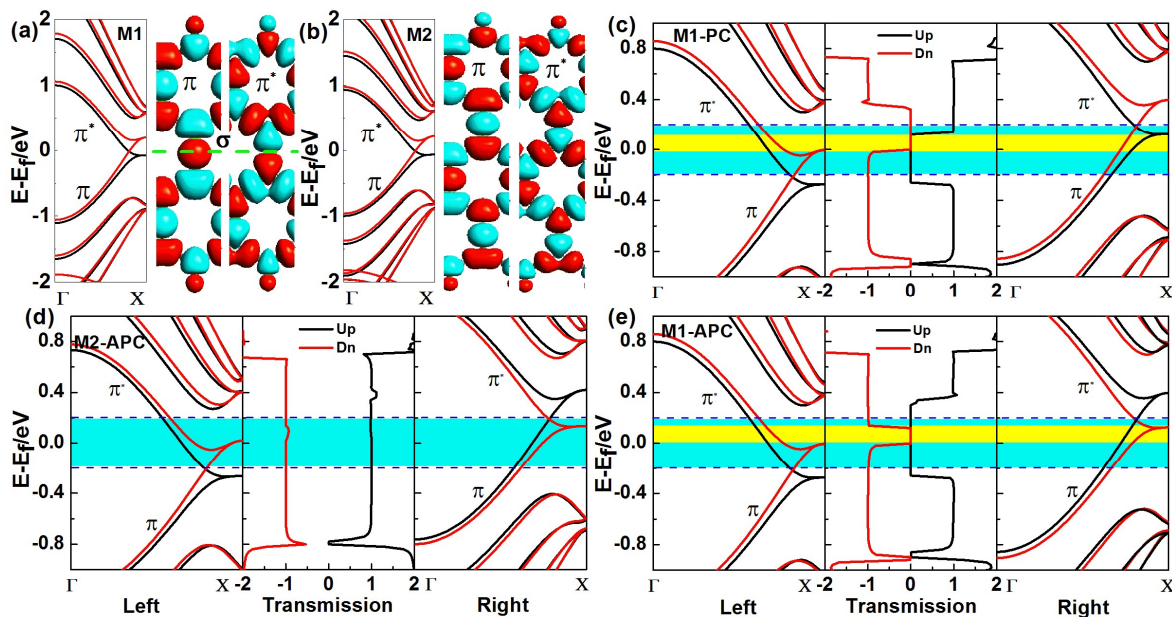
Fig. 4 Zhang et al.

Fig. 4 (Color online) (a) and (b) Band structures and wave functions (π and π^* subbands at Γ point) for F-4ZαGYNR-F and F-5ZαGYNR-F. The red and blue colors indicate positive and negative signs, respectively. The surface isovalue is 0.02. The green dashed line represents the σ mirror plane. The band structures for the left electrode (left panels), transmission spectra (middle panels), and the band structures for the right electrode (right panels) at V_b=0.4 V of (c) M1 in PC, (d) M2 in APC and (e) M1 in APC. The area between the blue dashed lines is the energy region contributes to the current, *i.e.* the bias window. The blue and yellow shades within bias window show the transmission spectrum and transmission gap, respectively.
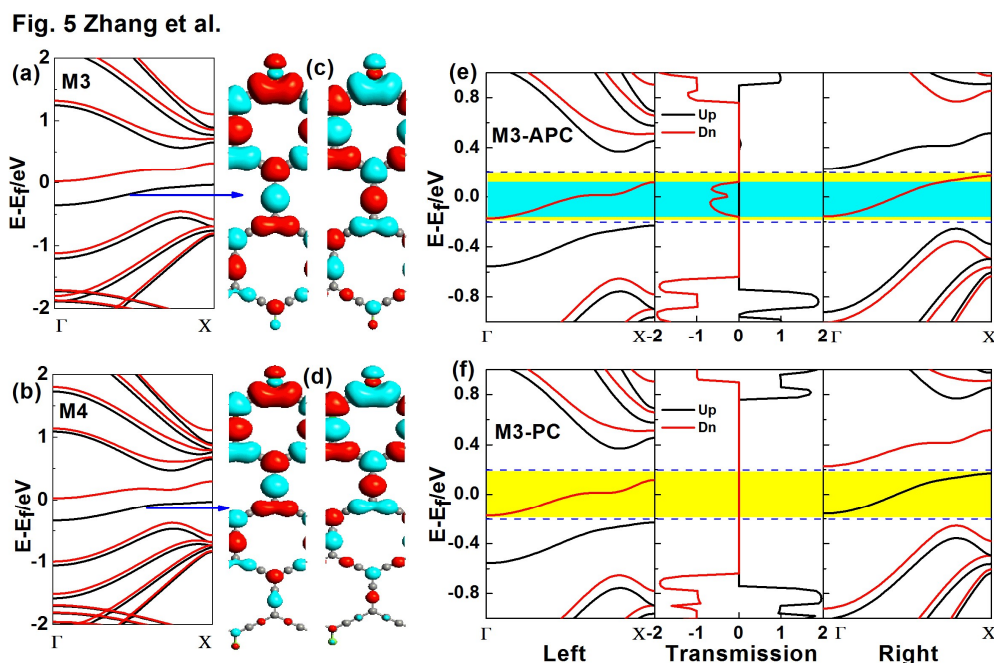

Fig. 5 Zhang et al.

Fig. 5 (Color online) (a) and (b) Band structures of F2-4ZαGYNR-F and F2-5ZαGYNR-F. (c) and (d) The wave function of spin-up and spin-down subbands near the Fermi level at Γ point. The red and blue colors indicate positive and negative signs, respectively. The surface isovalue is 0.02. (e) and (f) Band structures for the left electrode (left panels), transmission spectra (middle panels), and the band structures for the right electrode (right panels) of M3 device at V_b = 0.4 V in APC and PC, respectively. The region between the blue dashed lines is the bias window. The blue and yellow shades within the bias window show the transmission spectrum and transmission gap.
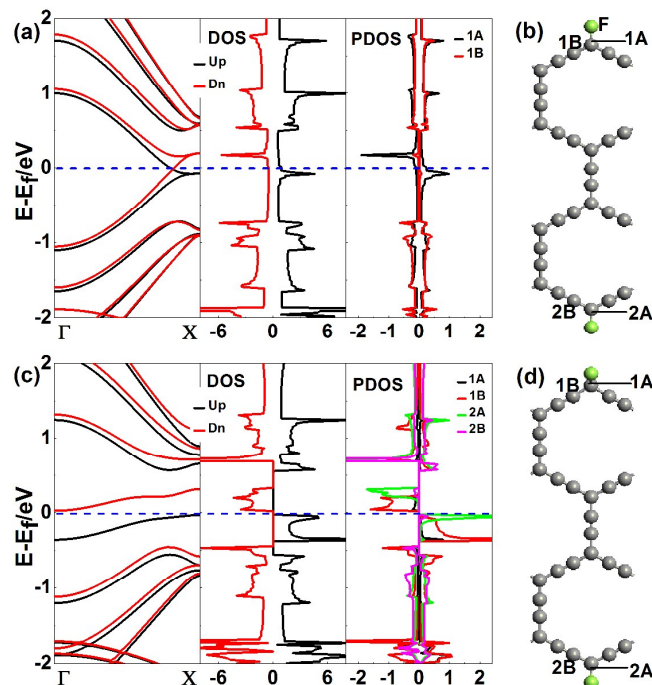
15

Fig. 6 Zhang et al.

Fig. 6 (Color online) (a) and (c) Band, DOS, and PDOS for F-4ZαGYNR-F and F2-4ZαGYNR-F. (b) and (d) The geometric structures of F-4ZαGYNR-F and F2-4ZαGYNR-F. The blue dashed line is the Fermi level. The A and B corresponding to the carbon atoms near them.
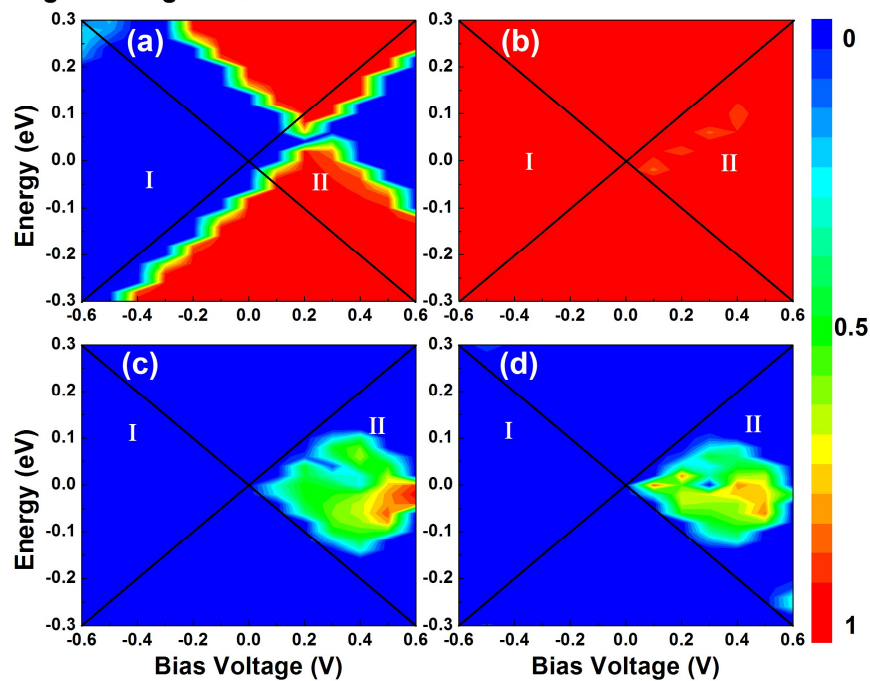
Fig. 7 Zhang et al.

Fig. 7 (Color online) The spin-resolved transmission spectrum as a function of electron energy and bias voltage for spin-down states of M1, M2, M3, and M4 in APC. The regions I and II between the black solid lines denote the negative and positive bias windows, respectively.

Graphical Abstract